Chen *et al. Cell Communication and Signaling* (2025) 23:238
https://doi.org/10.1186/s12964-025-02256-2

Cell Communication and Signaling

RESEARCH Open Access

The cancer-associated fibroblast facilitates YAP liquid-liquid phase separation to promote cancer cell stemness in HCC

Wei Chen[1,2†], Yanling Li[1†], Qiaodan Zhou[1], Wang Peng[1], Mengdie Cao[1], Yuchong Zhao[1], Zihan Yang[3], Si Xiong[1], Hai Huang[1], Luyao Liu[1], Shuya Bai[1,4*] and Bin Cheng[1,4*]

Abstract

Cancer stem cells (CSCs) are strongly associated with the refractory characteristics of Hepatocellular carcinoma (HCC). However, the complex interaction between CSCs and the tumor microenvironment remains incompletely understood. In this study, we identified a novel long non-coding RNA (lncRNA) NEAT1 in cancer-associated fibroblast (CAFs)-derived extracellular vesicles (EVs) that play a critical role in the induction of CSCs and HCC tumorigenesis. NEAT1 was significantly overexpressed in human HCC tissues. Furthermore, high expression of lncRNA NEAT1 in EVs was found to be associated with poor prognosis. Knockdown of NEAT1 in CAFs inhibited invasion, migration, and tumor growth. Mechanistically, NEAT1 promoted cancer cell stemness, including 3D spheroid formation, by facilitating the liquid-liquid phase separation (LLPS) of the transcription factor YAP. Specifically, NEAT1 is directly bound to the intrinsic disordered region in the YAP protein, promoting the formation of LLPS biomolecular condensates. Additionally, a positive correlation between NEAT1 and Nanog was observed in clinical HCC tissues. In conclusion, our findings reveal that NEAT1 promotes HCC carcinogenesis and CSC induction by facilitating the LLPS of the YAP protein.

Keywords Hepatocellular carcinoma, Long non-coding RNA, NEAT1, Extracellular vesicle, Liquid-liquid phase separation

Introduction

Hepatocellular carcinoma (HCC) is a prevalent cancer with high mortality rates globally. Despite the availability of various treatment options, including surgery, chemotherapy, immunotherapy, radiation, and interventional therapy, the 5-year overall survival rate remains below 50% [1]. Therefore, further investigations are crucial for fully understanding the molecular mechanisms underlying HCC pathogenesis.

The tumor microenvironment (TME) plays a critical role in the development and progression of HCC [2]. Comprising tumor cells, immune cells, cancer-associated fibroblasts (CAFs), blood vessels, and lymphatic vessels, the TME is closely associated with HCC [3, 4]. Among

[†]Wei Chen and Yanling Li contributed equally to this work.

*Correspondence:
Shuya Bai
18137370151@163.com
Bin Cheng
b.cheng@tjh.tjmu.edu.cn
[1]Department of Gastroenterology and Hepatology, Tongji Hospital, Tongji Medical College, Huazhong University of Science and Technology, Jiefang Road, No.1095, Wuhan 430030, China
[2]School of Life Sciences, The Chinese University of Hong Kong, Shatin, New Territories, Hong Kong 999077, China
[3]College of Basic Medical Sciences, Hubei University of Chinese Medicine, Huangjiahu West Road 16, Wuhan 430065, China
[4]Department of Gastroenterology, Tongji Hospital, Tongji Medical College, Huazhong University of Science and Technology, Jiefang Road, No.1095, Wuhan 430022, Hubei, China

these components, CAFs, the most abundant stromal cells in the TME, exert multiple effects on cancer cells and the surrounding stroma through direct cell contact or the release of paracrine cytokines and extracellular vesicles (EVs) [5]. Recent studies have demonstrated the involvement of CAF-derived exosomal circTBPL1 in breast cancer progression via the miR-653-5p/TPBG pathway [6]. Similarly, miR-3173-5p derived from CAF exosomes has been found to inhibit ferroptosis in pancreatic cancer cells by sponging ACSL4 [7]. Moreover, EVs, as natural carriers in the cancer microenvironment, facilitate the transfer of signaling molecules between distant cells, thereby modulating various cancer hallmarks, including proliferation, apoptosis, metastasis, and stemness capacity [8].

Emerging evidence suggests that liquid-liquid phase separation (LLPS) of RNA-binding proteins drives the formation of liquid droplet-like granules within cells [9]. LLPS is mediated by multivalent, weak interactions involving intrinsically disordered regions (IDRs), folded proteins, and scaffolding RNA molecules [10]. These LLPS condensates facilitate molecular assembly and enhance the activity of transcription factors, epigenetic regulators, and tumor suppressors [11]. In the nucleus, LLPS is crucial for heterochromatin formation and gene expression regulation. For instance, LEF1 can form IDR-dependent condensates with β-catenin, which are essential for β-catenin-dependent transcription [12]. Additionally, GATA2-AS1 has been shown to inhibit FUBP3 phase separation, thereby repressing neuroblastoma progression by modulating SUZ12 activity [13].

Long non-coding RNAs (lncRNAs) are recognized as key regulators of gene expression in humans [14]. lncRNA Nuclear enriched abundant transcript 1 (NEAT1) is located in the nucleus and maintains the structural integrity of paraspeckles. NEAT1 is a pan-cancer lncRNA that contributes to the development of various cancers and non-neoplastic diseases [15]. Recent findings have revealed that NEAT1 promotes the proliferation and metastasis of HCC and the self-renewal of liver cancer stem cells [16]. Furthermore, in other liver diseases, such as liver fibrosis and non-alcoholic fatty liver disease, lncRNA NEAT1 can influence the activation of hepatic stellate cells by regulating the expression of various miRNAs [17–19]. This regulatory process subsequently promotes changes in liver stiffness and functional alterations.

In this study, we investigated the significantly overexpressed lncRNA NEAT1 in human HCC tissues and explored its impact on the biological function of HCC cells. Additionally, we aimed to identify novel therapeutic targets for HCC and potential biomarkers for immunotherapy and prognosis.

Materials and methods

Patient liver tissue specimen and demographic information

We procured paraffin-embedded sections of liver tissues, including both tumorous and adjacent non-tumorous (3 cm away from the tumor border) specimens, from a cohort of 40 HCC patients who underwent curative resection at the Tongji Hospital, Huazhong University of Science and Technology (HUST, Wuhan, China), during the period spanning from 2013 to 2018. The clinical data pertaining to these specimens were meticulously recorded while ensuring the anonymity of the patients. The age range of the tumor patients is from 28 to 68 years old. All human experiments were approved by the ethics committee of Tongji Hospital (No. TJ-IRB20230430). Informed consent was obtained from all subjects. Prior to their inclusion, informed consent was diligently obtained from all participating subjects. In the event of unexpected situations during the surgical procedure, informed consent from family members may be required. The degree of tumor differentiation was rigorously assessed and categorized in accordance with the Edmondson grading system. (See Table 1).

This is a retrospective study focusing on the processing and analysis of patient specimens collected between 2013 and 2018. All patients included in the study received comprehensive and standardized treatment, and every procedure was meticulously conducted in strict accordance with ethical requirements. To identify eligible participants, we systematically reviewed hospital records from Tongji Hospital, specifically targeting patients who underwent liver cancer surgery between 2013 and 2018. For patients with accessible contact information, we initiated phone-based communications. During these conversations, we provided a detailed explanation of the study's objectives, methods, and potential benefit. Subsequently, we furnished them with comprehensive informed consent forms that clearly delineated the intended use of their archived tissue samples and clinical data and obtained their informed consent.

To anonymize patient information, we removed all direct identifiers such as names, addresses, and social security numbers from the collected data. We replaced them with unique codes. Regarding IRB compliance, we submitted a detailed protocol for review before the study began. The IRB approved our methods for sample collection, data handling, and anonymization. We also regularly reported progress to ensure ongoing adherence to ethical guidelines.

Cell lines and cell culture

The human hepatocellular carcinoma (HCC) cell lines, SNU398 and MHCC-97 H, were sourced from the reputable American Type Culture Collection (ATCC)

Table 1 The active CAFs related to clinicopathological features in HCC patients

Clinical features	High α-SMA (*n* = 24)	Low α-SMA (*n* = 16)	*p*-value
Age			
Young (< = median, 52)	16	9	0.52
Old (> median, 52)	8	7	
Gender			
male	20	11	0.44
Female	4	5	
Overall survival, median, months	17.3 months	38.2 months	***
Serum AFP (ng/ml)			
Low (< = 20)	7	9	0.10
High (> 20)	17	7	
Differentiation status			
Well differentiation	8	7	0.526
Moderately to poorly differentiation	16	9	
Tumor size			
Small (< = 5 cm)	10	3	0.17
Large (> 5 cm)	24	13	
TNM stage [a]			
Early stage (I-II)	13	12	0.48
Advanced stage (III-IV)	9	4	
Lymph node metastasis			
Absence	15	12	0.50
Presence	9	4	
Vascular infiltration			
Absence	16	12	0.72
Presence	8	4	

[a] AJCC/UICC staging system

*$p < 0.05$, ***$p < 0.001$, significant difference (χ2 test and Fisher's exact test)

located in Manassas, Virginia, USA. The 293T cell line is obtained from the Department of Gastroenterology and Hepatology, Tongji Hospital. These cell lines were propagated and maintained in an optimal environment utilizing Dulbecco's Modified Eagle's Medium (DMEM; GIBCO, Grand Island, NY, USA), fortified with 10% fetal bovine serum (FBS; GIBCO) at a temperature of 37 °C and under a controlled atmosphere containing 5% CO2. To ensure the integrity and purity of our experimental models, rigorous mycoplasma screening was performed using the Bimake mycoplasma detection kit, confirming the absence of mycoplasma contamination in all cell lines utilized. The absence of STR profiling for cell line authentication is a limitation of our study.

Extracellular vesicle isolation

We collected 100 ml of cell culture supernatant from each cell line and concentrated it using a 10 kDa filter. Subsequently, 10 ml of the concentrate was incubated with magnetic extracellular vesicle trap beads (Tymora Analytical Operations), following the manufacturer's protocol for 60 min with agitation. The supernatant was then discarded using a magnetic separator, and the beads were washed with PBS (4 °C, twice). The EVs were eluted through two 10-minute incubations with 100 mM trimethylamine (TEA, Millipore Sigma). Concurrently, a portion of the concentrated supernatant underwent Transmission Electron Microscopy (TEM) and western blot analysis to verify the presence of EV markers (CD9, CD81, TSG101).

Transmission electron microscopy (TEM)

Extracellular vesicles (EVs) were resuspended in 2% paraformaldehyde and deposited onto carbon formvar coated copper grids. These grids were subsequently stained with uranyl acetate to enhance contrast. For TEM analysis, the EVs were fixed overnight in 2% glutaraldehyde dissolved in 0.1 M phosphate buffer, followed by post-fixation in 2% osmium tetroxide for 1 h under identical buffer conditions. The specimens underwent a graded dehydration process using ethanol series and were then embedded in EM-bed resin (Electron Microscopy Sciences, Fort Washington, PA). The glass coverslip, if present, was dissolved in hydrofluoric acid. Ultrathin Sect. (100 nm) were meticulously cut using a Leica Ultracut EM UC7 ultramicrotome and further stained with uranyl acetate and lead citrate to improve visualization. The grids were examined at 80 kV on a JEOL JEM-1400 transmission electron microscope, and high-resolution images were captured using an AMT BioSprint 12 digital camera. In the Transmission Electron Microscopy (TEM) experiment, we did not add EV markers (CD9, CD81, TSG101). During the TEM process, we observed the membrane integrity of EVs and measured their diameter to determine that EVs were not damaged during the extraction.

Lentivirus production, transduction and plasmids construction

Lentivirus-mediated NEAT1 expression or silencing was achieved by the documented method [5] with some modifications. Briefly, for expression, the synthesized NEAT1 sequence was integrated into a pLKD-CMV-mcherry-2 A-Pur-U6-shRNA vector supplied by ObiO Technology. This vector's authenticity, along with the inserted NEAT1 sequence, was verified through DNA sequencing. Subsequently, this plasmid was co-transfected into 293T cells along with a lentiviral vector packaging system (ObiO Technology), utilizing Lipofectamine 3000 (Invitrogen™, L3000015), as the transfection reagent. The resulting lentiviruses, designated as NEAT1 expression vectors, were utilized to infect CAFs and NFs cells in the presence of polybrene (Sigma-Aldrich), followed by selection with puromycin. The modulation of NEAT1 expression levels in these cells was subsequently assessed through qRT-PCR. The siRNAs were designed and

produced by RiboBio (Guangzhou China). Additionally, to generate FLAG-tagged YAP expression vectors, full-length, truncated, or mutated YAP cDNA was subcloned into the pcDNA3.1-3×FLAG vector (ObiO Technology).

RNA isolation and reverse transcription quantitative PCR (RT-qPCR)

Total RNA was extracted from both cell lines and liver tissue specimens employing the TRIzol reagent (Invitrogen), followed by reverse transcription utilizing either random primers or specific lncRNA primers. Real-time quantitative PCR (qPCR) was then conducted using SYBR Premix (DRR041A, TaKaRa, Japan), adhering to a previously established protocol [20]. The RT-qPCR thermal cycling involves an initial denaturation at around 95 °C for 2–5 min. Then 30–40 cycles of denaturation (95 °C, 30–60 s), annealing (50–65 °C, 30–60 s), and extension (72 °C, 30–60 s), followed by a final extension at 72 °C for 5–10 min. GAPDH mRNA served as an internal control to normalize the qPCR data. When conducting RIP assay do we select U6 as the internal reference. For each gene, a standard curve was constructed using serially diluted standards, enabling the extrapolation of values for unknown samples. Both standards and samples were assayed in triplicate to ensure reproducibility and accuracy. The assay details and primer sequence presented in the Supplementary section (Supplementary Table S1).

Biotin-coupled probe RNA pull down assay

Biotinylated lncRNA NEAT1 pull down assays were performed as described earlier [20]. In brief, biotin-labeled lncRNA NEAT1 probes were introduced into 293T cells and incubated at 37 °C in a CO2-controlled environment for 60 min. Subsequently, the cells were fixed with methanol and lysed rapidly using 4 mL of Trizol reagent to extract total RNA, which was then sonicated. Following centrifugation (4 °C, 12000 g, 15 min), 50 µL of the supernatant served as the input material. Affinity-based capture of RNA fragments was achieved by incubating them with streptavidin magnetic dynabeads (Invitrogen, USA) at 4 °C overnight. The streptavidin magnetic beads were then isolated using a magnetic field, and the bound RNA-protein complexes were washed thoroughly with a wash buffer (4 °C, 3 min, twice). These complexes were subsequently eluted and purified using Trizol Reagent (Takara, Japan), preparing them for further downstream analysis. The sequences were in Supplementary section (Supplementary Table S1).

RNA FISH and Immunofluorescence

Fluorescent in situ hybridization (FISH) was conducted utilizing the RiboBio Fluorescent In-situ Hybridization Kit (Guangzhou China). Prior to hybridization, SNU-398 cells or paraffin-embedded tissue sections were fixed and permeabilized. Subsequently, NEAT1 probes (GenePharma, Supplementary Table S1) were hybridized to the samples overnight in a humidified chamber maintained at 37°C, with all steps performed under dark conditions to preserve fluorescence. The resulting images were captured using an Olympus FV1000 confocal microscope, where signals were detected through the 4′,6-diamidino-2-phenylindole (DAPI) and Cy3 channels. To facilitate visualization, cell nuclei were counterstained with DAPI.

Cell migration and invasion assay

The cell invasive and migratory ability was detected using an 8 µm pored, 6.5 mm polycarbonate transwell filter (Millipore, Billerica, MA, USA), according to our previous study [21]. For the migration assay, 5×10^4 cells were seeded onto the upper chamber of a transwell apparatus in serum-free DMEM. The lower chamber was filled with DMEM medium supplemented with 10% FBS to serve as a chemoattractant. Following incubation for 36–48 h, the non-migratory cells were removed by fixing the migrated cells with paraformaldehyde and staining them with a 4 g/L crystal violet solution for 30 min. Migrated cells were then counted using a microscope (Nikon, ECLIPSE Ti2). In the cell invasion assay, the upper chamber was first uniformly coated with a layer of Matrigel to mimic the extracellular matrix. The subsequent procedures were identical to those of the migration assay. Both migration and invasion experiments were performed in triplicate to ensure reproducibility and statistical significance.

Wound healing assays

First, we seeded the cells onto a 12-well plate until the cell density reached 100%. Then, we used a low-serum culture medium (with a fetal bovine serum concentration of 1%). A sterile pipette tip creates a scratch, mimicking a wound. Post - scratch, the debris is removed by gentle washing with PBS. Cells are then incubated, and their migratory response is monitored. Images are captured at regular intervals, often every 12 h. Using image analysis tools, the width of the remaining wound area is measured. The rate of wound closure over time quantifies cell migration.

Colony-formation assay

Cells were seeded in 6-well plates at a density of 1000 cells per well to facilitate colony formation. After approximately 10 days of incubation, the colonies were fixed with 4% methanol for 20 min to ensure their integrity. Subsequently, the colonies were stained with crystal violet (C0121, Beyotime, China) for clear visualization and counting. The results obtained were presented as the mean number of colonies ± standard deviation (SD),

providing a quantitative assessment of colony-forming ability.

Sphere formation assay

The cells were seeded into 24-well low attachment plates (Corning, NY, USA) and cultured in a specialized tumor sphere medium. This medium consisted of DMEM/F12 (cat#11320033; GIBCO), supplemented with 1% penicillin/streptomycin for antimicrobial protection, 1x B27 supplement (cat# 17504-044; GIBCO) for essential nutrients, 20 ng/ml EGF (cat# PHG0311; GIBCO) and 10 ng/ml bFGF (cat# PHG0266; GIBCO) to promote cell growth and differentiation, and 1% methyl cellulose (cat#M0262; Sigma-Aldrich) to enhance sphere formation. To maintain optimal growth conditions, fresh medium was replenished every 3–4 days. Spheres were regularly monitored and counted using microscopy for quantitative analysis.

Western blot analysis

Western blot analysis was performed as described previously [22]. Primary and secondary antibodies were list in Supplementary section (Supplementary Table S2). Additionally, monoclonal mouse anti-α-tubulin or β-actin antibody was employed as an internal control to ensure the reliability and consistency of the experimental results. Histone H3 is used as the internal reference protein for the cell nucleus.

Immunohistochemistry (IHC)

For histochemical verification, we used the specified antibodies, which are listed in Supplementary Table 2. The paraffin-embedded tissue sections underwent pre-treatment involving heating at 60 °C for two hours, subsequent hydration, and antigen retrieval through steaming in Tris-based Antigen Unmasking Solution (VectorLabs Cat#H3301-250) for 20 min, followed by cooling to room temperature. To block endogenous peroxidase, pseudoperoxidase, and alkaline phosphatase in formalin-fixed, paraffin-embedded (FFPE) sections, Bloxall (VectorsLabs Cat # SP6000-100) was applied for 10 min. After washing with IHC wash buffer (PBS containing 0.1% Tween 20) for 5 min, the sections were incubated with 2.5% normal goat serum (cat# 50197Z, Thermo Fisher Scientific) for 20 min to prevent non-specific binding. The antibodies were diluted in goat serum as per previously mentioned concentrations and incubated with the sections overnight at 4 °C in a humidified chamber. Following a 5-minute wash in wash buffer (4 °C), the sections were incubated with ImmPRESS Universal Polymer Reagent (VectorLabs Cat# MP-7451) for 30 min. After two washes in wash buffer, the sections were treated with ImmPACT DAB EqV peroxidase substrate solution (VectorLabs Cat#SK4103-400) for 5 min, rinsed twice in wash buffer for 5 min each, and then briefly rinsed in tap water. Counterstaining was achieved using Hematoxylin QS counterstain (VectorLabs Cat# H3404-100) for 60 s, followed by rinsing in tap water. The slides were then dehydrated using standard methods and mounted with Vectamount permanent mounting medium (VectorLabs Cat# H5000-60). Notably, the blocking and antibody incubations were performed using 2.5% horse serum (cat#31874 Invitrogen), adhering to the manufacturer's instructions.

To ensure objectivity, the assessment of IHC staining scores was independently conducted by two blinded pathologists, unaware of the associated clinical data. The immunostaining intensity was scored on a scale of 0 to 3: 0 (negative), 1 (weak), 2 (medium), or 3 (strong). The percentage of positive cells was evaluated on a scale of 0 to 4: 0 (negative), 1 (1-25%), 2 (26-50%), 3 (51-75%), or 4 (76-100%). The final immuno-activity scores were calculated by multiplying the above two scores, resulting in an overall score that ranges from 0 ~ 12. Each case was ultimately considered "negative" if the final score ranges from 0 ~ 3, and "positive" if the final score ranges from 4 ~ 12.

RNA biology assay

RNA pull-down assay and RIP assay were performed as previously described with minor modifications [23]. The cell lysates utilized for the pull-down assay were meticulously prepared using the ProteaPrep Zwitterionic Cell Lysis Kit (Protea®), which includes an Anti-RNase agent to ensure RNA integrity. This lysis buffer was further supplemented with a comprehensive Protease Inhibitor Cocktail, Phosphatase Inhibitor Cocktail, as well as the addition of Panobinostat and Methylstat to inhibit specific enzymatic activities and preserve protein interactions. The resulting protein complexes were subsequently eluted and efficiently digested with Immobilized Trypsin (Promega), ensuring precise cleavage for subsequent analysis. The digested proteins were then subjected to a western blot assay for detailed characterization and identification.

Phase separation assay in cells

MHCC-97 h and SNU398 cells, engineered to express YAP-GFP, were cultured on coverslips until they adhered securely. Following adhesion, the cells underwent a thorough washing process with PBS twice, followed by fixation with 4% paraformaldehyde dissolved in PBS for a duration of 10 min. Subsequently, the cells were washed an additional two times with PBS to remove any residual fixative. Utilizing confocal microscopy (OLYMPUS, FV3000), the cells were meticulously analyzed, and those distinct punctate structures with diameters exceeding 0.5 μm were clearly defined as YAP-GFP puncta. We utilized the "3D_Objects_Counter" in the FIJI plugin to count the number of fluorescent puncta. In our cell

phase - separation experiments, the reagent used for the positive control was polyethylene glycol – 400 (PEG400), PEG300 and PEG800, while hexanediol (Hex – 1,6) was used for the negative control.

Fluorescence recovery after photobleaching (FRAP)

FRAP experiments were conducted with precision on an OLYMPUS FV3000 confocal microscope, equipped with a 60× oil immersion objective lens. The GFP tag was located at the C terminus of YAP. During these experiments, droplets were subjected to photobleaching using a 488-nm laser at 50% power for a duration of 0.5 s. Immediately following photobleaching, time-lapse images were captured every three seconds over a period of 5 s to monitor the recovery process. For in vivo experiments, the FRAP assays were performed under physiological conditions at 37 °C within a specialized live-cell imaging chamber, also utilizing the OLYMPUS FV3000 confocal microscope. Here, droplets were selectively photobleached with a 488-nm laser pulse, applied at 50% intensity for 0.5 s. The subsequent recovery from photobleaching was meticulously recorded over the specified time interval. The analysis of the obtained recovery curves was performed using the advanced image processing capabilities of FIJI/ImageJ software, ensuring accurate and reliable quantification of the fluorescence recovery dynamics.

Animals and treatments

Male BALB/C nude mice (Huafukang Bio, Beijing) aged 6–7 weeks were employed in the experiments. A total of 40 mice were used. The mice, on average, weighed around 25 g. As for the housing conditions, the mice were housed in a temperature - controlled environment (around 22 ± 2 °C) with a 12 - hour light/dark cycle. They were kept in individually ventilated cages (IVC) filled with standard rodent bedding material. In the context of the subcutaneously implanted tumor model, 5×10^5 cells of MHCC-97 H and SNU398, which had been transfected with the specified lentivirus, were resuspended in a 50 µl mixture of PBS and Matrigel (Corning, NY, USA) at a ratio of 1:1. Subsequently, the cell suspension was injected into the right-back flanks of the mice. The anatomical structure of this area is relatively distinct, making it easy to identify and precisely locate. And the right-back flanks region is endowed with a rich vascular network, which can supply ample oxygen and nutrients to the inoculated tumor cells, facilitating their survival, proliferation, and growth [24, 25].

Following the implantation of the cell lines, the mice were subject to daily monitoring. We measured the size of subcutaneous tumors in the mice once every three days. For the surviving mice, they were euthanized (neck dislocation), and their tumors were collected at the predetermined end point of observation. In the case of BALB/C nude mice, the observation end point was set at 28 days after cell implantation. The tumors were then embedded in paraffin and subsequently stained with H&E for histological analysis.

In our study, we set several humane endpoints for tumor - burdened mice. We monitored their physical state and behavior. If tumor growth severely distressed the mice, like causing mobility problems, it was a potential endpoint. When the tumor volume exceeded 20% of the body weight, the experiment should stop. In our experiment, the maximum tumor volume was 2500 mm^3, still under the limit. We also watched for physiological signs. A weight loss of over 20% from the start, labored breathing, a hunched posture, or long - term loss of appetite were all red flags. When multiple such signs appeared, it meant the tumor burden was too much. Then, we'd act according to ethical rules to protect the mice's welfare. All animal experiments were duly approved by the Ethics Committee of Tongji Hospital, Tongji Medical College, Huazhong University of Science and Technology, ensuring compliance with ethical standards and regulations governing animal research.

Statistical methods

In each experiment, data were systematically presented as mean ± SD. Each experiment was performed three times independently. Statistical significance was firmly established at $P < 0.05$, ensuring that any observed differences were of genuine importance. To this end, we meticulously analyzed the data using R (RStudio, version 4.0.2) and GraphPad Prism (GraphPad, 9.0 software), carefully selecting the most appropriate statistical tests tailored to the specific data characteristics. The software used for graphic processing is Image J (Elice IRI/Loci Lab, Version 1.5xf). For datasets displaying approximately normal distribution, we leveraged the paired Student's t-test for pairwise comparisons and one-way ANOVA for multiple groups. The Tukey's Honestly Significant Difference (HSD) Test was used after the one-way ANOVA. For those deviating from normality, we applied the Wilcoxon signed-rank test to accurately analyze the data. Furthermore, for assessing survival outcomes, we employed the log-rank test to compare survival curves across groups. We utilize the Spearman's Rank Correlation Coefficient Test in examining the correlation between the expression levels of protein in the tissue of cancer patients. We employed the Shapiro - Wilk Test to evaluate the normality of the data. Throughout the analysis, we maintained a rigorous standard, considering $P < 0.05$ as the threshold for statistical significance.

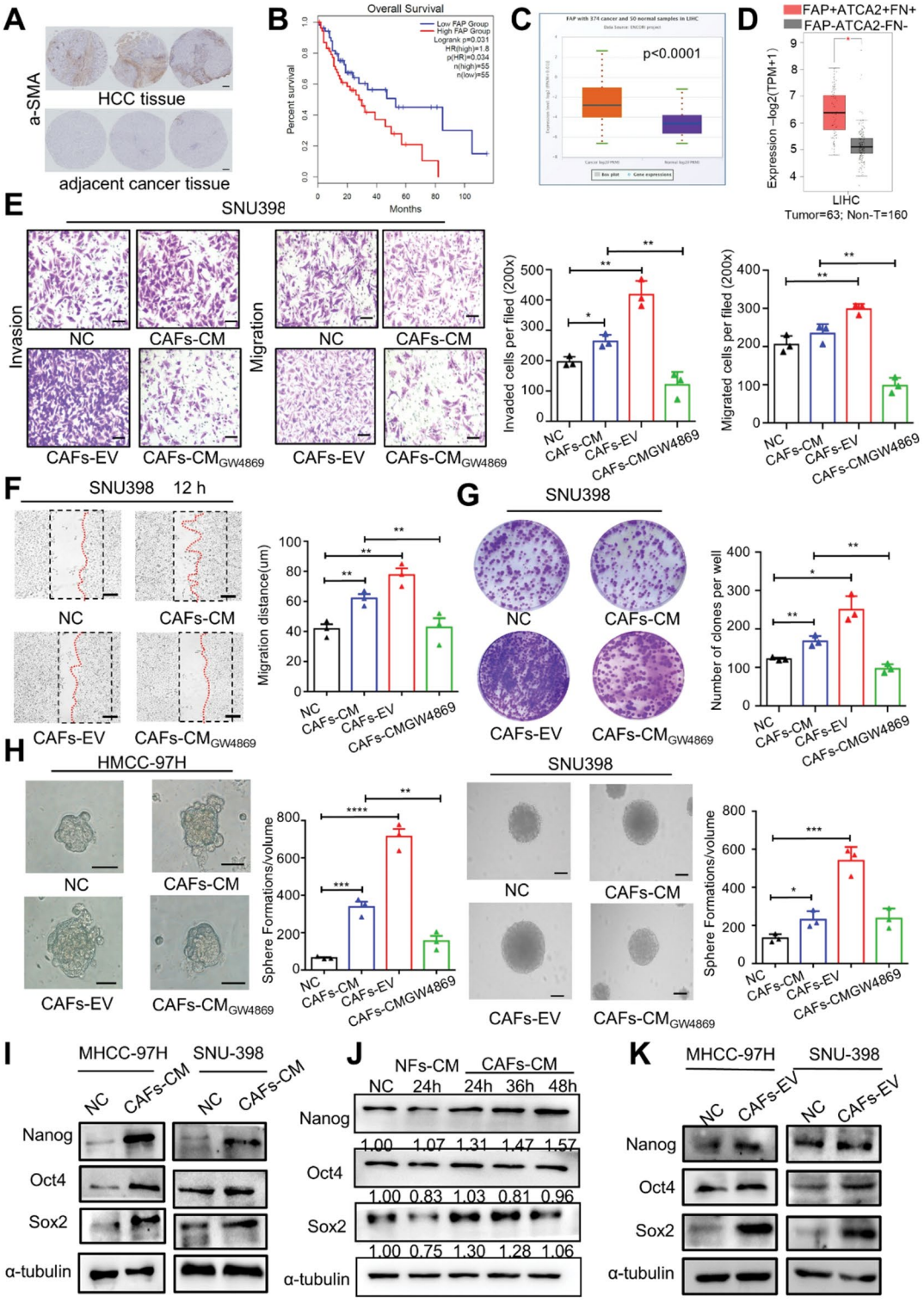

Fig. 1 (See legend on next page.)

Results

Isolation and identification of extracellular vesicles derived from primary NFs and CAFs

CAFs were isolated from tumor tissue samples of HCC patients, while NFs were purified from liver tissues adjacent to hepatic hemangiomas. Microscopic examination revealed similar morphologies between NFs and CAFs, although NFs appeared thinner and more elongated with

(See figure on previous page.)

Fig. 1 CAFs promoted CSCs stemness capacity via extracellular vesicles in HCC. (**A**) IHC detected of a-SMA protein expression in the tissue microarray of HCC patients. Scale bars: 200 μm. (**B**) overall survival (OS) of HCC patients in the FAP-high and FAP-low groups. (**C**) The expression of FAP in 374 cancer and 50 normal samples in HCC by bioinformatics analysis. (**D**) The expression of FAP + ACTA2 + FN + cells and the FAP-ACTA2-FN- cells in HCC tissue and adjacent tissue. Transwell assays (**E**) and wound healing assay (**F**) were performed to examine the effects of CAFs-CM, CAFs-EV and the GW4869-treated CAFs-CM on HCC cell invasion and migration. Scale bars: 50 μm. (**G**) The colony formation assay was performed to examine the effect of CAFs on HCC cell proliferation. (**H**) The 3D spheroid formation assay was performed to examine the effect of CAFs on HCC cell stemness capacity. Scale bars: 20 μm. (**I** & **J**) Western blot assay was performed to detect the expression of stemness-associated genes in CAFs-CM treatment (**K**) and CAFs-EVs treatment. Each experiment was performed three times independently and the results are presented as mean ± SD. Student's t-test was used to analyze the data; $^{*}p < 0.05$, $^{**}p < 0.01$, $^{***}p < 0.001$, $^{****}p < 0.0001$

fewer cell processes (Fig. S1A). To confirm the activation status of CAFs, we examined the expression of α-SMA, vimentin, and FAP, known markers of CAF activation, in NFs and CAFs using western blot analysis (Fig. S1B) and immunofluorescence staining (Fig. S1C). The results demonstrated higher expression levels of α-SMA, vimentin, and FAP in CAFs compared to NFs.

To investigate the effects of extracellular vesicles (EVs) derived from CAFs and NFs on HCC cells, we isolated and characterized EVs from both cell types. The nanoparticle tracking analysis (NTA) was performed to determine the size distribution and concentration of CAFs and NFs-derived EVs (Fig. S1D). The majority of isolated EVs had diameters ranging from 80 to 150 nm, and the concentration ranged from 7×10^6 to 9×10^6 particles/ml. Transmission electron microscopy revealed that EVs in the supernatants of CAFs and NFs exhibited a spherical morphology with sizes ranging from 50 to 120 nm (Fig. S1E). Additionally, Western blot analysis confirmed the presence of EV markers (CD9, CD81, TSG101, and CD63) in both purified EV samples (Fig. S1F). These findings indicate that the size and shape of EVs derived from CAFs and NFs were similar.

CAFs promote CSC stemness capacity via extracellular vesicles in HCC

To investigate the role of CAFs in promoting HCC carcinogenesis and induction of liver CSCs, we examined the expression of the activated fibroblast marker α-SMA in an HCC tissue microarray (Fig. 1A). Our findings revealed a higher presence of α-SMA positive CAFs in HCC tumor tissue compared to adjacent tissue (Fig. S1G). Analysis of the TCGA database showed that higher expression of fibroblast activation protein (FAP) was associated with poor prognosis (Fig. 1B), and the expression of FAP was higher in HCC tumor tissue than in adjacent tissue (Fig. 1C). We used the GEPIA2 to analyze the $FAP^+ACTA2^+FN^+$ genes in HCC tissue and adjacent tissue (Fig. 1D), and found significantly higher expression of these triple-positive genes in tumor tissue.

We treated HCC cell lines, SNU398 and MHCC-97 H, with CAFs cell culture supernatant (CAFs-CM), CAFs-derived extracellular vesicles (CAFs-EV), and CAFs conditioned medium treated with the EVs release inhibitor GW4869 (CAFs-CM GW4869). Transwell migration and wound healing assays revealed enhanced migration of both MHCC-97 H and SNU398 cells in the CAFs-EV group and CAFs-CM group, which was significantly inhibited when HCC cells were treated with CAFs-CM GW4869 (Fig. 1E, Fig. S2A & B). Clonogenic assays demonstrated that EVs derived from CAF culture supernatant promoted stronger clonogenic ability in HCC cells (Fig. 1G, Fig. S2C). Similarly, 3D spheroid formation assays indicated that CAF culture supernatant-derived EVs enhanced the stemness capacity of HCC cells (Fig. 1H).

Treatment of HCC cells with CAF culture supernatant resulted in a significant increase in the expression of CSC stemness-related genes (Nanog, Sox2, Oct4) (Fig. 1I). Furthermore, treatment of HCC cells with CAFs or NFs culture supernatant over a time gradient showed that the expression of Nanog, Sox2, and Oct4 increased with time (Fig. 1J). To confirm the effect of EVs in the CAFs culture supernatant, we isolated the EVs and treated HCC cells with 40 ng of CAFs-EV. As expected, the expression of Nanog, Sox2, and Oct4 increased (Fig. 1K). These findings collectively demonstrate that EVs derived from CAFs promote the migration, invasion, and stemness capacity of HCC cells.

CAF-derived EVs exhibit upregulated expression of lncRNA NEAT1

Extracellular vesicles (EVs) are known to contain various forms of RNA and DNA [26]. To investigate the underlying mechanisms contributing to HCC progression, we utilized bioinformatics analysis (exoRBase, http://www.exorbase.org/) to detect lncRNA enrichment in EVs derived from serum samples of HCC patients and healthy volunteers (Fig. 2A and B). The analysis revealed 640 upregulated lncRNAs in EVs obtained from patient serum. We focused on these enriched lncRNAs, as they may have significant tumor-promoting potential and serve as treatment and diagnostic biomarkers. Subsequently, the top four upregulated lncRNAs with known annotations were selected for further validation using qRT-PCR (Fig. 2C). Among them, lncRNA NEAT1 showed increased expression in EVs derived from CAFs compared to NFs. Additionally, NEAT1 expression was significantly higher in CAFs compared to NFs (Fig. S3A). Further qRT-PCR analysis identified the highest expression of NEAT1 in

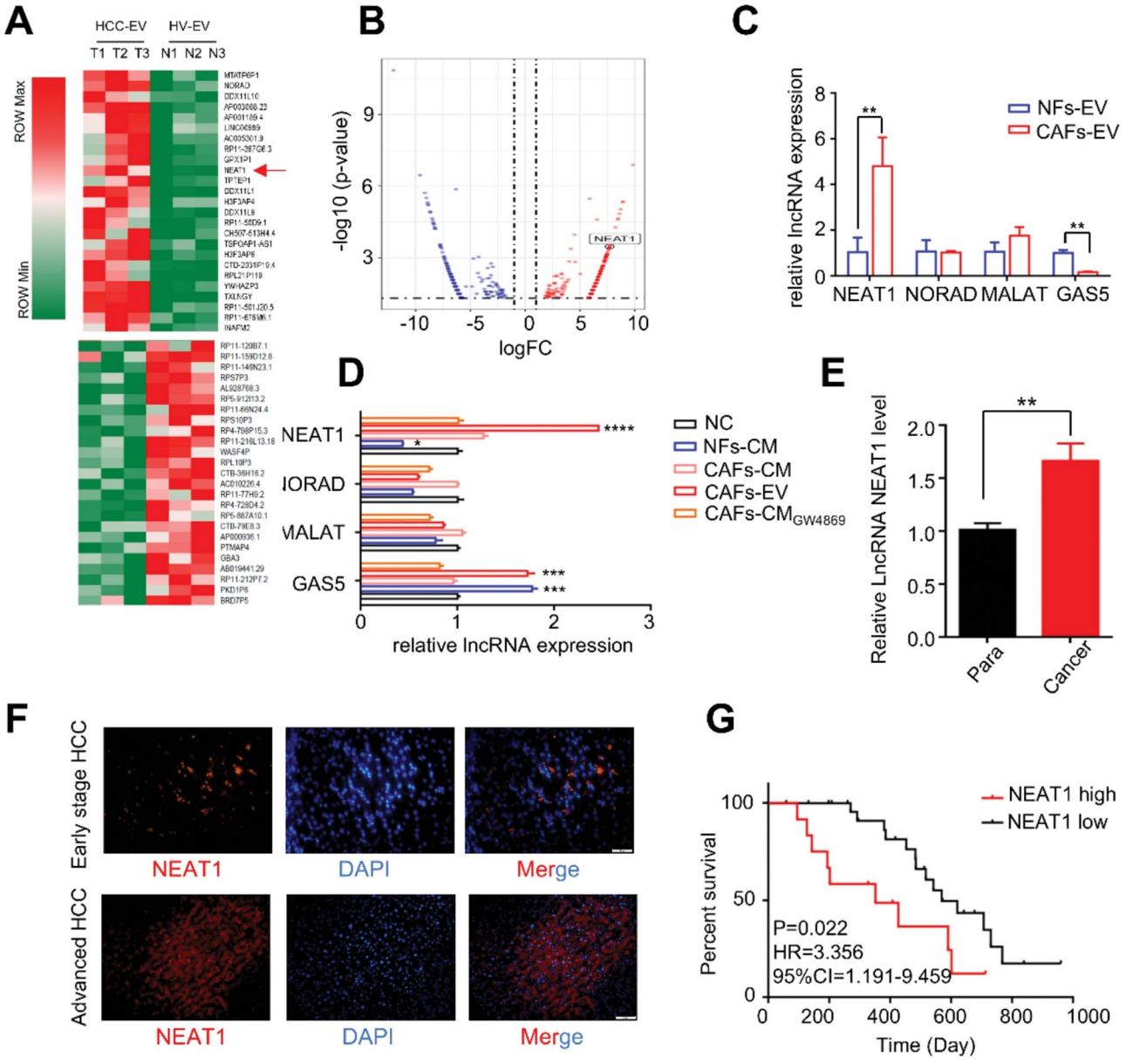

Fig. 2 CAFs derived EVs exhibit upregulated expression of lncRNA NEAT1. (**A**) the heatmap of the lncRNA expression from HCC patients' serum extracellular vesicles (HCC-EVs) and the healthy volunteers' serum extracellular vesicles (HV-EVs) by bioinformatics (exoRBase, http://www.exorbase.org/). (**B**) the volcano plot of the different lncRNA expression in HCC-EVs and HV-EVs. (**C**) The top 4 alternative lncRNA were examined by qRT-PCR in CAFS-EVs and NFs-EVs. (**D**) The lncRNA was examined by qRT-PCR in different treatments by CAFs and NFs. (**E**) the expression of NEAT1 in HCC tissue and para-cancer tissue. (**F**) the NEAT1 was examined by immunofluorescence in early-stage HCC tissue and advanced HCC tissue. (**G**) overall survival (OS) of HCC patients in the NEAT1-high and NEAT1-low groups. Each experiment was performed three times independently and the results are presented as mean ± SD. Student's t-test was used to analyze the data; $^{**}p < 0.01$. Scale bars: 20 μm

the CAFs-EVs treated group compared to other groups (Fig. 2D).

To assess the clinical relevance of NEAT1, we compared its expression in HCC patient tissue and para-tumor tissue using qRT-PCR in our cohort and a public database (Fig. 2E, Fig. S3B). The results demonstrated a significant upregulation of NEAT1 in cancer tissue, suggesting its association with HCC cell stemness abilities. Fluorescence in situ hybridization (FISH) analysis of a tissue microarray of HCC further confirmed these findings (Fig. 2F). Moreover, the 5-year overall survival (OS) of the NEAT1 high group was significantly lower than the NEAT1 low group (Fig. 2G). Therefore, NEAT1 was selected for further functional evaluation to determine its biological significance in HCC.

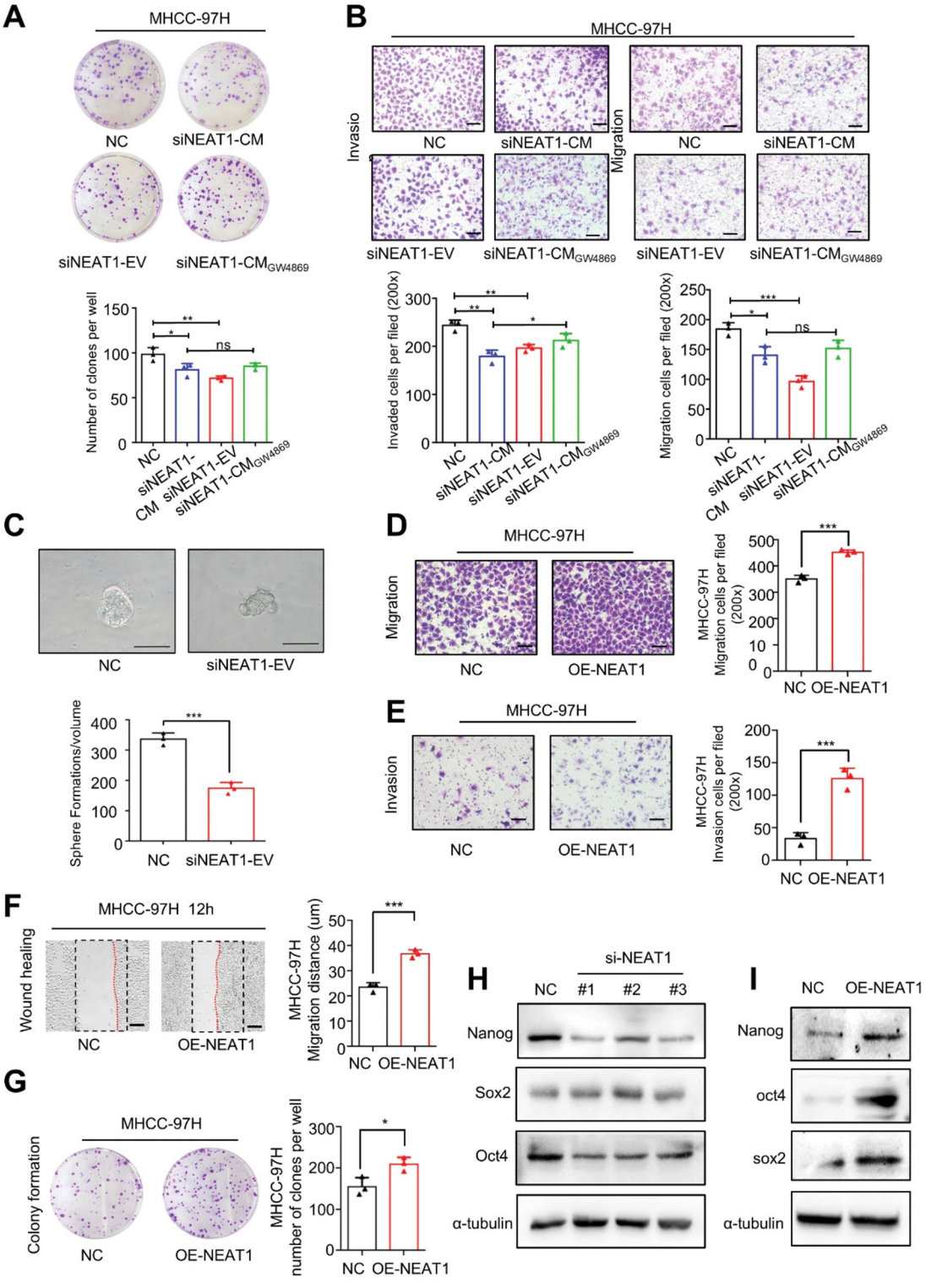

Fig. 3 (See legend on next page.)

NEAT1 in CAFs derived EVs promotes HCC stemness capacity

To further elucidate the role of NEAT1 in cell stemness capacity, we employed siRNAs to down-regulate NEAT1 in CAFs. The cell culture supernatant (siNEAT1-CM), EVs (siNEAT1-EV), and CAFs conditioned medium treated with GW4869 (siNEAT1-CM GW4869) were applied to MHCC-97 H and SNU398 cells. Transwell

(See figure on previous page.)

Fig. 3 NEAT1 in CAFs derived EVs promotes HCC stemness capacity. (**A**) The colony formation assay was performed to examine the effect of NEAT1 on HCC cell proliferation. (**B**) Transwell assays were performed to examine the effects of si-NEAT1 treated CAFs and si-NEAT1 CAF-EVs on HCC cell invasion and migration. Scale bars: 50 μm. (**C**) The 3D spheroid formation assay was performed to examine the effect of si-NEAT1 CAF-EVs on HCC cell stemness capacity. Scale bars: 20 μm. (**D** & **E**) Transwell assays were performed to examine the effects of overexpression NEAT1 on HCC cell invasion and migration. Scale bars: 50 μm. (**F**) The wound healing assay was performed to examine the effects of overexpression NEAT1 on HCC cell growth and differentiation. Scale bars: 50 μm. (**G**) The colony formation assay was performed to examine the effect of overexpression NEAT1 on HCC cell proliferation. (**H** & **I**) Western blot assay was performed to detect the expression of cancer stemness-associated genes after silencing NEAT1 or overexpression NEAT1. Each experiment was performed three times independently and the results are presented as mean ± SD. Student's t-test was used to analyze the data; ns. No sense, $^{*}p < 0.05$, $^{**}p < 0.01$, $^{***}p < 0.001$

migration and cloning formation assays revealed a decrease in the migration of both MHCC-97 H and SNU398 cells in the siNEAT1-EV group and siNEAT1-CM group, which was significantly rescued when HCC cells were treated with GW4869 (Fig. 3A and B, Fig. S3C & S3D). Similarly, 3D spheroid formation assays indicated that siNEAT1 decreased the stemness capacity of HCC cells (Fig. 3C).

Conversely, we overexpressed NEAT1 in MHCC-97 H and SNU-398 cells by transfecting NEAT1 plasmids. Transwell migration/invasion and wound-healing assays demonstrated that NEAT1 overexpression significantly increased the migration and invasion of both HCC cell lines compared to the control group (Fig. 3D and F, Fig. S4A– S4C). Colony formation assays further indicated that NEAT1 overexpression enhanced cell growth and anchorage-independent growth of HCC cells compared to the controls (Fig. 3G, Fig. S4D). To confirm that NEAT1 regulates cancer stemness-associated genes (Nanog, Sox2, and Oct4), we performed western blot assays and qRT-PCR to assess the expression of these genes after NEAT1 silencing or overexpression NEAT1 (Fig. S5A & S5B, Fig. 3H and I). The results demonstrated that knockdown of NEAT1 decreased the protein expression of Nanog, Sox2, and Oct4 compared to the control group. Collectively, these findings suggest that NEAT1 plays a critical role in cell motility and stemness capacity.

NEAT1 interacts with YAP protein to promote HCC stemness capacity

Recent studies have demonstrated that lncRNAs in the cell nucleus can facilitate the function of transcriptional factors by acting as scaffolds for liquid-liquid phase separation (LLPS) [27]. Therefore, we aimed to determine the downstream signaling pathway of NEAT1 in cancer cells. Through bioinformatics analysis (GSE159905), we compared the mRNA expression between cells transfected with scramble plasmid and cells transfected with si-NEAT1 (Fig. 4A). The results revealed that knockdown of NEAT1 led to the upregulation of 615 mRNAs and the downregulation of 2364 mRNAs. The most relevant signaling pathways affected were the Wnt signaling pathway, the Hippo signaling pathway, the mTOR signaling pathway, and the AMPK signaling pathway. To identify the specific biomolecule interacting with NEAT1, we performed RNA pull-down assays (Fig. 4B). The results demonstrated a clear interaction between NEAT1 and the YAP protein, suggesting that NEAT1 may interact with YAP. Subsequently, we conducted RNA Immunoprecipitation (RIP) assays to further confirm the interaction between NEAT1 and the YAP protein (Fig. 4C). Interestingly, the RIP assay revealed a significant increase in NEAT1 in the YAP pulldown samples compared to the U6 control group.

To investigate the contribution of NEAT1 in facilitating the LLPS process of the YAP protein, we analyzed the distribution of YAP protein and NEAT1 in the CAFs-EVs treated group (Fig. 4D, Fig. S6A). Confocal microscopy revealed that the biotin-labeled NEAT1 (Red) precisely coincided with the YAP protein (Green). As expected, discrete puncta of YAP protein were observed in cells treated with CAFs-EVs. These findings suggest that NEAT1 can facilitate the LLPS process of the YAP protein and promote the Hippo signaling pathway, but not other signaling pathways.

The LLPS condensation of YAP can promote the HCC stemness ability

By conducting bioinformatics analyses of the YAP protein sequence, we discovered that YAP is highly disordered and contains three intrinsically disordered regions (IDR-1 to IDR-3) throughout its sequence (Fig. 4E, Fig. S6B). These IDRs are known to mediate protein LLPS, suggesting that YAP may undergo LLPS. Indeed, exogenously expressed YAP-GFP formed puncta in the cytoplasm when treated with the LLPS agonist polyethylene glycol-400 (PEG400), while treatment with the LLPS disruptor 1,6-Hexanediol (Hex-1,6) failed to induce puncta formation (Fig. S7). Furthermore, YAP-GFP puncta exhibited fusion, a highly dynamic process, as demonstrated by fluorescence recovery after photobleaching (FRAP) assay (Fig. 4F, Fig. S8A & S8B). Over time, small puncta of YAP-GFP fused into larger ones, indicating dynamic exchange of molecules between liquid droplets and the surrounding solution (Fig. 4G, Video 1). These findings strongly suggest that YAP undergoes LLPS in cells.

To investigate the in vivo function of YAP LLPS, we treated MHCC-97 H and SNU398 cells overexpressing YAP-GFP with PEG400 and Hex-1,6. Transwell migration

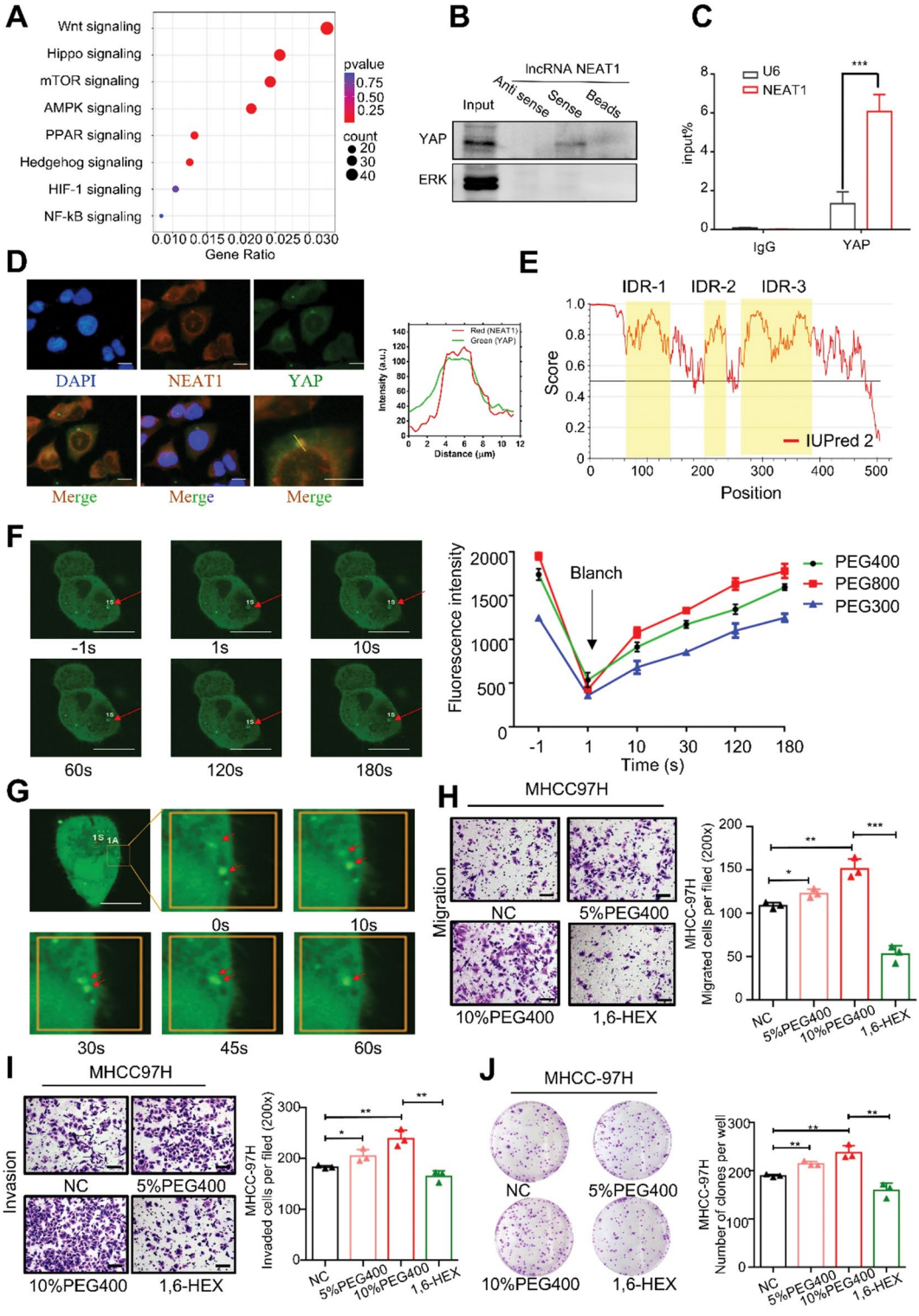

Fig. 4 (See legend on next page.)

and invasion assays revealed that HCC cells treated with PEG400 exhibited significantly increased migration and invasion compared to the control group, while Hex-1,6 treatment decreased migration and invasion ability (Fig. 4H and I, Fig. S9A, B). Cloning formation and wound healing assays demonstrated that PEG400 stimulation enhanced cell growth and anchorage-independent growth of HCC cells compared to the controls, whereas

(See figure on previous page.)

Fig. 4 NEAT1 interacts with YAP protein to promote HCC stemness capacity. (**A**) The bubble plot of pathway enrichment analysis highlights the strongly differentially enriched pathways in si-NEAT1 with the scramble group using the Kyoto Encyclopedia of Genes and Genomes with adjusted. (**B**) the RNA pull-down assay was performed to analyze the direct interaction between YAP and NEAT1. (**C**) the RIP assay was performed to examine the interaction between YAP and NEAT1. (**D**) FISH analysis of YAP puncta in the indicated NEAT1 overexpression HCC cells, and overlapped with the NEAT1. The fluorescence intensities of the red fluorescence (NEAT1) and the green fluorescence (YAP) along the yellow line were obtained. Scale bars: 20 μm. (**E**) The schematic illustration of YAP shows domains. Predictions of disordered regions by prion-like amino acid composition. (**F**) the fluorescence intensity of YAP-GFP droplets recovered after bleaching during FRAP assay. Time 0 indicates the photobleaching pulse. Scale bars: 20 μm (**G**) Time-series fluorescence microscopy analysis of YAP-GFP droplets fused during the phase separation process. Scale bars: 20 μm (**H** & **I**) Transwell assays were performed to examine the effects of PEG400 and Hex-1,6 on HCC cell invasion and migration. Scale bars: 50 μm (**J**) The colony formation assay was performed to examine the effect of PEG400 and Hex-1,6 on HCC cell proliferation. Each experiment was performed three times independently and the results are presented as mean ± SD. Student's t-test was used to analyze the data; *$p < 0.05$, **$p < 0.01$, ***$p < 0.001$

Hex-1,6 had the opposite effect (Fig. 4J, Fig. S9C, Fig. S10A, B). These data further support the notion that YAP1 activity is facilitated by phase separation, which regulates YAP's transcriptional activation.

NEAT1 in CAFs-EVs promotes the LLPS of YAP

Since regulating the NEAT1 facilitated the LLPS of YAP in HCC cells, we proceeded to investigate whether NEAT1 in CAFs-EVs could promote HCC development by regulating the LLPS process of YAP. As depicted in Fig. 5A, extracellular vesicles derived from CAFs facilitated the phase separation of YAP protein in HCC cells compared to the NC group and the NFs-EV treated group. To further explore the role of NEAT1 in CAFs-EVs in a concentration-dependent manner, HCC cells were treated with CAFs-EVs at different concentrations. The results demonstrated that the formation of YAP droplets was dependent on the concentration of CAFs-EVs (Fig. 5B). Furthermore, when we silenced NEAT1 in CAFs and treated HCC cells with siNEAT1-EVs, the small puncta of YAP-GFP were no longer observed (Fig. 5C). These findings suggest that NEAT1 in CAFs-EVs facilitates the LLPS process of YAP and promotes HCC development.

NEAT1 regulates tumor stemness capacity in HCC in vivo

To investigate the tumorgenicity of NEAT1 in vivo, the control group and sh-NEAT1 group HCC cell line, MHCC-97 H, and SNU-398 were injected subcutaneously into 4-weeks- old male BALB/c nude mice. As expected, the mean volume of tumor nodules in the sh-NEAT1 group was significantly lower than that in the control group (Fig. 6A and B). The day 28 tumor weight is 2.70 ± 0.17 g vs. 0.32 ± 0.04 g in SNU-398 cell line, 2.84 ± 0.08 g vs. 0.20 ± 0.05 g in MHCC-97 H cell line ($p < 0.0001$, t-test). In addition, we analyzed the cancer cell stemness-associated gene in the subcutaneous tumor tissue to explore the stem capacity of HCC cells and found that the down-regulated NEAT1 could reduce the Nanog, Sox2 and Oct4 expression (Fig. 6C). Furthermore, we obtained tumor tissues for immunohistochemical staining, and we also found that interfering the expression of NEAT1 in HCC cells could significantly reduce the expression of Nanog and YAP (Fig. 6D).

In this study, we investigated the significantly overexpressed lncRNA NEAT1 in human HCC tissues and explored its impact on the biological function of HCC cells. In molecular mechanism, we found that CAFs-derived EVs are rich in lncRNA NEAT1, which can be transported to HCC cells and promote liquid-liquid phase separation of YAP protein, thus promoting the stemness capacity of HCC (Fig. 7). We aimed to identify novel therapeutic targets for HCC and potential biomarkers for immunotherapy and prognosis.

Discussion

As the key components of the tumor microenvironment, cancer-associated fibroblasts (CAFs) play a crucial role in maintaining the stemness capacity of hepatocellular carcinoma (HCC) [28]. However, the specific effects and underlying mechanisms of CAFs have not been thoroughly investigated. Recent studies have highlighted the interaction between CAFs and surrounding tumor cells through the secretion of extracellular vesicles (EVs), enabling indirect cell-to-cell contact and influencing the biological functions of tumor cells [5, 29]. Our findings confirm these observations. However, the lack of additional labeling of EV markers (CD9, CD81, TSG101) in the Transmission Electron Microscopy examination of exosomes is a limitation of our study. In our study, CAFs were isolated and cultured in vitro, and CAFs-EVs were collected for co-culture with HCC cells. Subsequent experiments demonstrated that CAFs-EVs significantly enhanced cell proliferation and stemness capacity in HCC cells, indicating that CAFs secrete EVs to accelerate cancer development in HCC. Furthermore, we identified various contents within CAFs-EVs, with long non-coding RNA (lncRNA) emerging as one of the most significant components. Through bioinformatics analysis and RT-qPCR analysis, we identified a novel lncRNA, NEAT1, which was particularly enriched in CAFs-EVs. Deletion of NEAT1 partially reversed the promoting effects of CAFs-EVs on HCC cell stemness capacity. These results suggest that NEAT1 in CAFs-EVs plays a crucial role in driving cancer development in HCC. Moreover, our

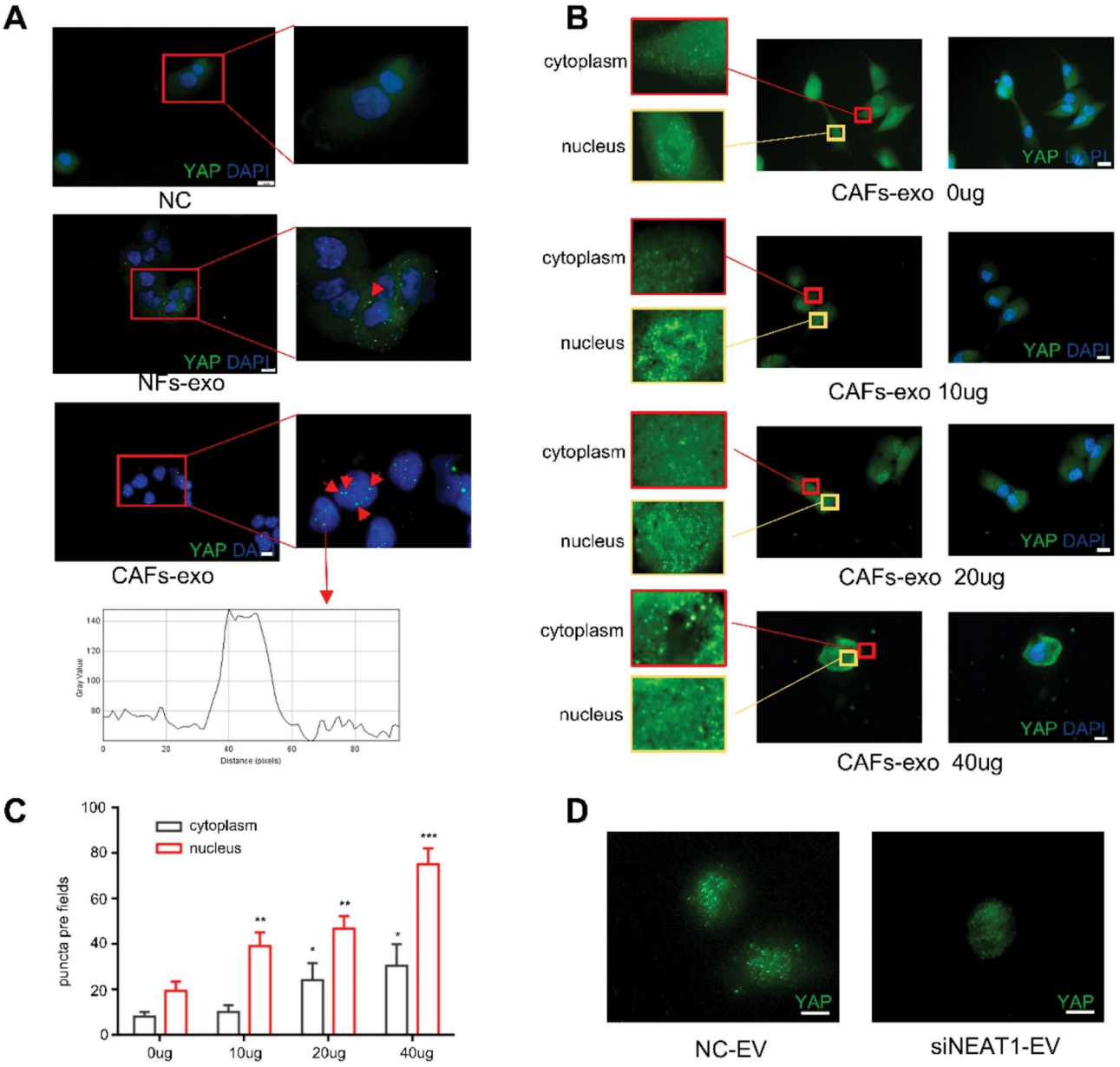

Fig. 5 The NEAT1 in CAFS-EV can promote the LLPS of YAP. (**A**) Endogenous YAP puncta were detected using anti-YAP antibody in HCC cells treated with CAFs-EVs or NFs-EVs. The bottom figure displays the fluorescence intensity of YAP puncta along the red line. Scale bars: 20 μm. (**B**, **C**) Phase-separation assay of NEAT1 in vivo showing droplet formation of YAP by treated with CAFs-EVs in concentration-dependent. Scale bars: 20 μm. (**D**) the phase-separation assay was performed to examine the effect of the YAP LLPS process by siNEAT1-EVs treated in HCC cells. Scale bars: 20 μm. Each experiment was performed three times independently and the results are presented as mean ± SD. Student's t-test was used to analyze the data; $^{*}p < 0.05$, $^{**}p < 0.01$, $^{***}p < 0.001$

findings indicate that NEAT1 in extracellular vesicles from patient serum could serve as a novel predictive molecular marker.

Accumulating evidence from prior investigations has established that lncRNA NEAT1 acts as a pivotal regulator of exosome biogenesis in hepatocellular carcinoma cells. Specifically, modulation of NEAT1 expression elicits a marked upregulation of exosome secretion, accompanied by a concurrent decrease in the intraluminal levels of miR-634, miR-638, and miR-3960 [30]. These molecular alterations collectively contribute to the enhanced invasive and migratory phenotypes of neoplastic cells. Moreover, the NEAT1-KIF11/CDKN2A signaling axis has been identified as a critical pathway in decelerating tumor cell senescence, thereby promoting oncogenic progression [31].

Our findings are consistent with these previous reports, providing additional validation for NEAT1's role in

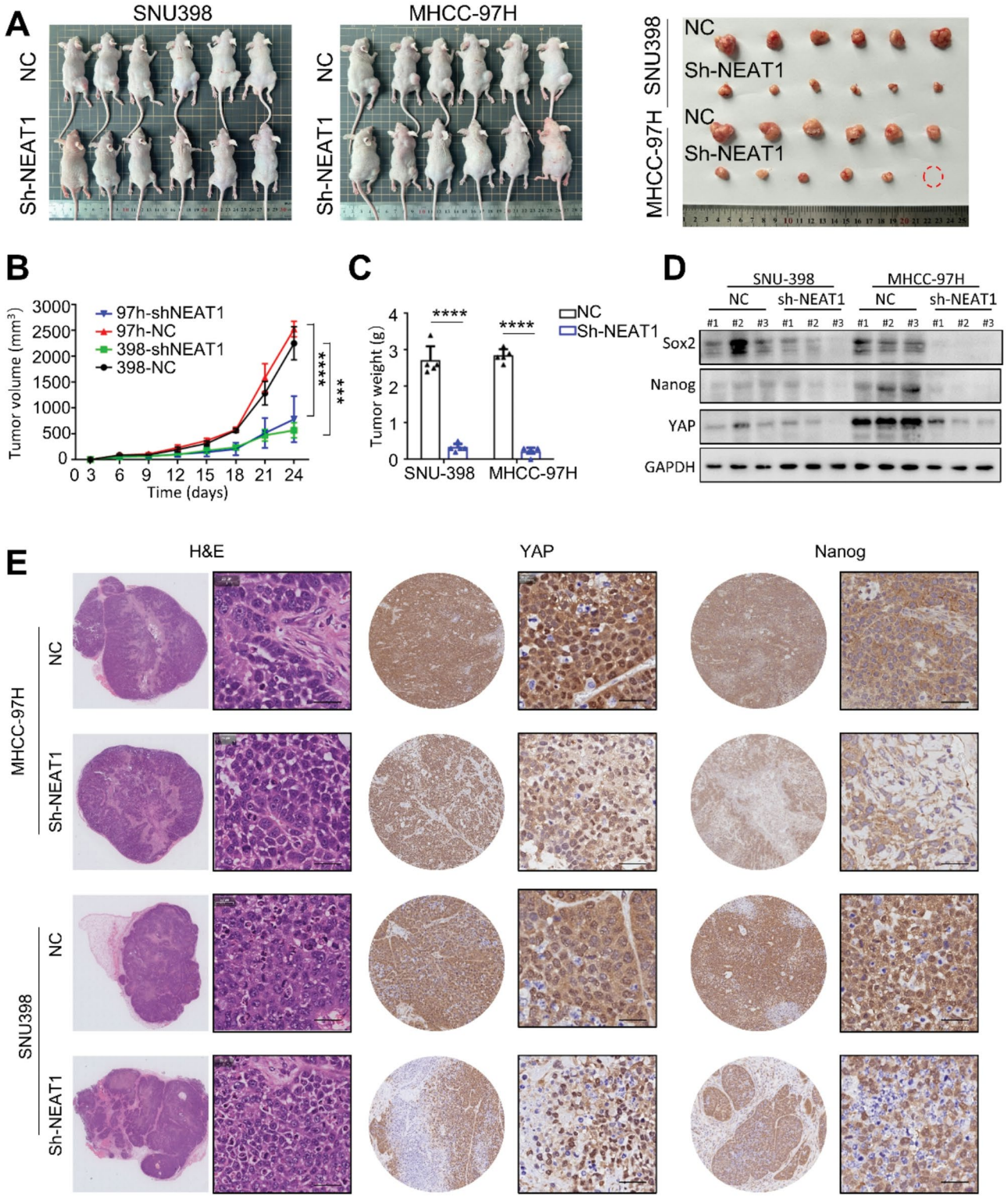

Fig. 6 NEAT1 regulates tumor stemness capacity in HCC in vivo. (**A**) sh-NEAT1 and control group SNU398 and MHCC-97 H cell lines were subcutaneously injected into the BALB/c mice. (**B**) The tumor volume and (**C**) the tumor weight from each group were tested. (**D**) Western blot assay showing the stemness-associated gene (Nanog and Sox2) and YAP expression in tumor tissue. (**E**) The representative images of IHC staining of YAP and Nanog. The picture on the left is a different magnification of the one on the right. Bars: 20 μm. Each experiment was performed three times independently and the results are presented as mean ± SD. Student's t-test was used to analyze the data; ****$p < 0.0001$

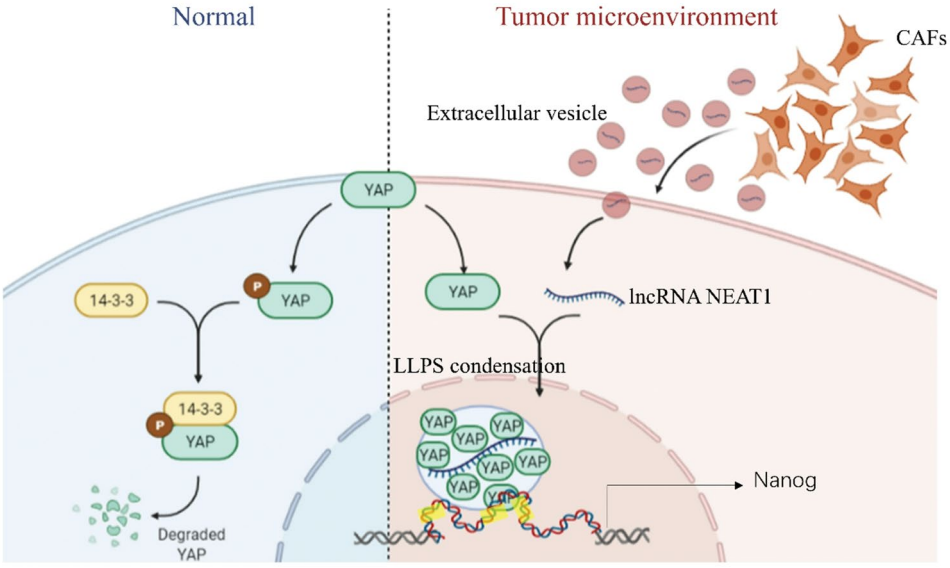

Fig. 7 Schematic diagram. NEAT1 enhanced cancer cell stemness characteristics through enabling the liquid-liquid phase separation of the transcription factor YAP. Precisely, NEAT1 directly attaches to the inherent disordered part of the YAP protein, thereby inducing the creation of LLPS biomolecular condensates

potentiating HCC malignancy. Notably, our study unveils a novel mechanism by demonstrating that CAF-derived exosomes serve as an exogenous source of NEAT1 in tumor cells. Through a series of regulatory mechanisms, we successfully suppressed NEAT1 expression in tumor cells, thereby inhibiting the phase separation of YAP protein. These results not only expand the current understanding of NEAT1's multifaceted functions in HCC but also identify potential therapeutic targets for intervening in tumor progression.

The mechanisms underlying the occurrence, organization, and properties of liquid-liquid phase separation (LLPS) condensates have long been elusive. However, recent years have witnessed significant advancements in our understanding of the molecular basis of cancer [32, 33]. It is now evident that a wide range of these condensates form through LLPS, leading to the emergence of complex multiphase coexistence within cells [34]. Notably, recent studies have unveiled that LLPS transcriptional condensates can assemble numerous transcription factors (TFs), co-factors, and RNA Pol II at transcriptional promoters [35]. The Hippo/YAP signaling pathway serves as a critical regulator in controlling cancer cell growth, stem cell activity, and innate immunity. YAP has been shown to interact with various transcription factors and can function at both transcriptional promoter and enhancer regions in the genome. The LLPS condensates harbor distinct protein sets that contribute to YAP's ability to redistribute into the nucleus. Within the nucleus, YAP droplets have been demonstrated to reorganize the genome, thereby driving long-term expression of YAP target genes [36].

Amino acid sequence analysis of YAP has revealed the presence of an intrinsically disordered region (IDR), endowing the protein with remarkable flexibility and dynamic conformational plasticity. Distinct from conventional protein domains with stable, well-defined 3D structures, IDRs lack a fixed folded state under physiological conditions [34]. Despite their disordered nature, these regions are integral to a multitude of biological processes, including cellular signal transduction, gene regulatory networks, and intricate protein - protein interaction cascades [32, 37]. Notably, prior research has established that TAZ, a transcription coactivator functioning as a key binding partner of YAP, can physically interact with YAP to form a heteromeric complex. In the presence of specific scaffold proteins or RNAs, this YAP/TAZ complex undergoes a coordinated phase separation event, highlighting the critical role of these disordered regions in driving liquid - liquid phase separation phenomena essential for cellular function and regulation [38]. These evidences confirm that the phase-separated droplets we observed are not composed of a single type of protein or nucleic acid. Instead, they are formed by the interactions of multiple proteins, with the binding of different protein domains to each other, collectively creating a relatively stable droplet structure. The YAP protein phase-separated droplets promoted by CAF-EVs in liver cancer cells also do not consist solely of the YAP protein. This represents a limitation of our study, and the protein interactions involved merit further exploration.

The LLPS of key proteins in tumor cells plays a crucial role in the progression of numerous tumors [39, 40]. The phase separation of various transcription factors

can sequester organelles or enhance the malignant capabilities of tumor cells by binding to enhancers [41]. Our study conclusively demonstrates that exosomes derived from cancer - associated fibroblasts (CAFs) in liver cancer can promote the liquid - liquid phase separation (LLPS) of YAP protein in liver cancer cells. Mechanistically, we identified that lncRNA NEAT1 in exosomes can act as a scaffold protein, binding to YAP protein and subsequently facilitating the phase separation process of YAP protein, augmenting the "stemness" ability of liver cancer cells. In this study, from the perspective of CAFs in the tumor microenvironment promoting the stemness of liver cancer cells and using exosomes as carriers, we newly elucidated the mechanism of phase separation in liver cancer cells, which is highly innovative and cutting-edge.

In this study, we employed PEG400 and Hex-1,6 to modulate the LLPS process of YAP and investigate its role in HCC development. Our results confirmed that YAP protein formed droplet-like condensates upon treatment with PEG400. Facilitating the LLPS of YAP significantly increased cell migration, invasion, and stemness capacity, whereas inhibition of LLPS with Hex-1,6 had the opposite effect. Moreover, in the presence of CAFs or treatment with CAFs-EVs, the LLPS of YAP occurred in a dose-dependent manner, indicating the crucial role of CAFs-EVs in regulating YAP LLPS. Subsequently, we discovered that NEAT1, present in CAFs-derived extracellular vesicles, interacts with YAP and promotes YAP phase separation, thereby acting as a positive regulator of cancer cell stemness capacity. NEAT1 accumulation in YAP condensates contributes to the formation of well-shaped droplets and recruitment of additional YAP. RNA pull-down and RIP assays demonstrated the direct binding of NEAT1 to YAP protein.

Our study has demonstrated that NEAT1 within CAFs-EVs can promote the phase separation of YAP protein in cells. However, the specific molecular mechanisms underlying this process require further investigation. Current research has shown that during the formation of nuclear paraspeckles, NEAT1 acts as a scaffold, facilitating the assembly of proteins such as NONO, RBM14, and SFPQ into liquid phase-separated structures [42, 43]. As a long non-coding RNA, NEAT1 folds at the paraspeckle assembly (B block), forming a stable structure with free ends outward and folded ends inward [36]. During this process, various proteins can bind to specific bases of NEAT1, thereby promoting the formation of protein droplets. However, further investigation is required to elucidate the mechanisms underlying the formation of NEAT1/YAP liquid droplets and the potential involvement of other key proteins or nucleic acids in these droplets.

Based on the molecular mechanisms underlying NEAT1-induce LLPS, a variety of targeted intervention strategies can be exploited to achieve therapeutic effects against tumors. Antisense oligonucleotides (ASOs) can be rationally designed to be complementary to specific sequences of NEAT1. Upon cellular entry, these ASOs form stable duplexes with NEAT1, thereby obstructing its normal biological functions [44]. The resulting NEAT1 - ASO complexes are subsequently degraded via endogenous cellular RNA - degradation pathways. In the context of hepatocellular carcinom, ASOs can be encapsulated within lipid - based nanoparticles, enabling targeted delivery to liver cancer cells. This targeted delivery strategy minimizes off - target effects and enhances the therapeutic index, optimizing the potential clinical utility of ASO - based therapies [45]. Similarly, CRISPR - Cas9 gene - editing technology offers a powerful approach for precisely targeting and modifying the NEAT1 gene locus in HCC cells. By introducing site - specific double - strand breaks within the NEAT1 gene, the cellular DNA repair machinery can be exploited to delete or disrupt the gene, effectively ablating NEAT1 expression. Despite its promise, the safe and efficient delivery of CRISPR - Cas9 components, including the Cas9 protein or mRNA and guide RNA, to liver cancer cells remains a significant technical challenge that requires further investigation and optimization.

This research endeavor is constrained by several notable limitations, with the primary weakness residing in the constrained and retrospective nature of the HCC samples utilized. As a retrospective cohort study, this research has certain value in exploring the mechanisms related to the fibroblast activation marker α-SMA in liver cancer tissues. However, the relatively small sample size, consisting of only 40 liver cancer patients, would impact the reliability and generalizability of the study results. When investigating the relationship between the degree of fibroblast activation in liver cancer and the clinical outcomes of liver cancer patients, the small sample may fail to identify some subtle yet clinically significant associations, potentially leading to false-negative results. Therefore, to obtain more comprehensive and robust conclusions, it is necessary to further increase the sample size of enrolled patients in future research. Furthermore, the absence of the utilization of patient-derived tumor xenograft (PDX) models, which closely mimic the genuine physiological conditions of human beings, may undermine the clinical relevance and future applicability of our findings.

Conclusion

Collectively, our data reveal that lncRNA NEAT1 in CAFs derived extracellular vesicles promoted HCC cell stemness by facilitating the liquid-liquid phase separation (LLPS) of the transcription factor YAP, providing a

potential prognostic marker and therapeutic target for HCC.

Supplementary Information

The online version contains supplementary material available at https://doi.org/10.1186/s12964-025-02256-2.

Supplementary Material 1

Supplementary Material 2

Acknowledgements
We thank the Huazhong University of Science and Technology, Analytical and Testing Center, medical subcenter for technical support. We would like to express our sincere gratitude to Dr. Wang Ronghua from the Department of Gastroenterology, Tongji Hospital, for providing us with cell support.

Author contributions
W.C, YC.Z, and B.C conceived and designed the study. MD.C, SY.B and LY.L performed the experiments. W.C, LY.L and S.X analyzed the data. W.C designed the probes sequences. W.C, YC.Z and B.C wrote and revised the paper. W.C, SY.B, QD.Z, ZH.Y, W.P, H.H and B.C saw and verified all the raw data. All authors read and approved the final manuscript.

Funding
This work was supported by the National Science Foundation of China (No. 81974380, No.82173318 and No. 82203812).

Data availability
All data that support the findings in this study are available from the corresponding author upon reasonable request.

Declarations

Ethics approval and consent to participate
All work related to human tissues was preapproved by the ethics committee of Tongji Hospital, Tongji Medical College, Huazhong University of Science and Technology (HUST, Wuhan, China), and this study was conducted in accordance with the Helsinki Declaration. All animal experiments were performed in accordance with the Animal Research: Reporting of In Vivo Experiments (ARRIVE) guidelines and also approved by the Animal Ethics Committee of Tongji Hospital. Written informed consent was obtained from the patients or families of the donors.

Consent for publication
We obtained Consent for publication specifically from all patients included in this research.

Competing interests
The authors declare no competing interests.

Received: 8 April 2025 / Accepted: 19 May 2025
Published online: 24 May 2025

References

1. Sung H, et al. Global Cancer statistics 2020: GLOBOCAN estimates of incidence and mortality worldwide for 36 cancers in 185 countries. CA Cancer J Clin. 2021;71(3):209–49.
2. Donne R, Lujambio A. The liver cancer immune microenvironment: therapeutic implications for hepatocellular carcinoma. Hepatology. 2023;77(5):1773–96.
3. Ruf B, Heinrich B, Greten TF. Immunobiology and immunotherapy of HCC: spotlight on innate and innate-like immune cells. Cell Mol Immunol. 2021;18(1):112–27.
4. Zhu GQ, et al. CD36(+) cancer-associated fibroblasts provide immunosuppressive microenvironment for hepatocellular carcinoma via secretion of macrophage migration inhibitory factor. Cell Discov. 2023;9(1):25.
5. Zhang Z, et al. Loss of Exosomal miR-320a from cancer-associated fibroblasts contributes to HCC proliferation and metastasis. Cancer Lett. 2017;397:33–42.
6. Ye F, et al. Cancer-associated fibroblasts facilitate breast cancer progression through Exosomal circTBPL1-mediated intercellular communication. Cell Death Dis. 2023;14(7):471.
7. Qi R, et al. Cancer-associated fibroblasts suppress ferroptosis and induce gemcitabine resistance in pancreatic cancer cells by secreting exosome-derived ACSL4-targeting MiRNAs. Drug Resist Updat. 2023;68:100960.
8. Huang H, et al. RAB27A-dependent release of exosomes by liver cancer stem cells induces Nanog expression in their differentiated progenies and confers regorafenib resistance. J Gastroenterol Hepatol. 2021;36(12):3429–37.
9. Zhang JZ, Mehta S, Zhang J. Liquid-liquid phase separation: a principal organizer of the cell's biochemical activity architecture. Trends Pharmacol Sci. 2021;42(10):845–56.
10. Shin Y, et al. Spatiotemporal control of intracellular phase transitions using Light-Activated optodroplets. Cell. 2017;168(1–2):159–e17114.
11. Lu Y, et al. Phase separation of TAZ compartmentalizes the transcription machinery to promote gene expression. Nat Cell Biol. 2020;22(4):453–64.
12. Zhao B et al. LEF1 enhances β-catenin transactivation through IDR-dependent liquid-liquid phase separation. Life Sci Alliance, 2023;6(11).
13. Wang X, et al. Therapeutic targeting of FUBP3 phase separation by GATA2-AS1 inhibits malate-aspartate shuttle and neuroblastoma progression via modulating SUZ12 activity. Oncogene. 2023;42(36):2673–87.
14. Herman AB, Tsitsipatis D, Gorospe M. Integrated LncRNA function upon genomic and epigenomic regulation. Mol Cell. 2022;82(12):2252–66.
15. Adriaens C, Marine JC. NEAT1-containing paraspeckles: central hubs in stress response and tumor formation. Cell Cycle. 2017;16(2):137–8.
16. Koyama S et al. NEAT1 is required for the expression of the liver Cancer stem cell marker CD44. Int J Mol Sci, 2020;21(6).
17. Sun Y, et al. LncRNA NEAT1-MicroRNA-140 axis exacerbates nonalcoholic fatty liver through interrupting AMPK/SREBP-1 signaling. Biochem Biophys Res Commun. 2019;516(2):584–90.
18. Kong Y, et al. The LncRNA NEAT1/miR-29b/Atg9a axis regulates IGFBPrP1-induced autophagy and activation of mouse hepatic stellate cells. Life Sci. 2019;237:116902.
19. Bu FT, et al. LncRNA NEAT1: shedding light on mechanisms and opportunities in liver diseases. Liver Int. 2020;40(11):2612–26.
20. Wang X, et al. Musashi2 contributes to the maintenance of CD44v6 + liver cancer stem cells via notch1 signaling pathway. J Exp Clin Cancer Res. 2019;38(1):505.
21. Xie Z, et al. Exosome-delivered CD44v6/C1QBP complex drives pancreatic cancer liver metastasis by promoting fibrotic liver microenvironment. Gut. 2022;71(3):568–79.
22. Chen W et al. CD44v6 + hepatocellular carcinoma cells maintain stemness properties through Met/cJun/Nanog Signaling. Stem Cells Int, 2022: p. 5853707.
23. Huang C, Wang Y. Downregulation of METTL14 improves postmenopausal osteoporosis via IGF2BP1 dependent posttranscriptional Silencing of SMAD1. Cell Death Dis. 2022;13(11):919.
24. Liang X, et al. Breaking the tumor chronic inflammation balance with a programmable release and Multi-Stimulation engineering scaffold for potent immunotherapy. Adv Sci (Weinh). 2024;11(28):e2401377.
25. Meyblum L et al. Local and distant response to intratumoral immunotherapy assessed by ImmunoPET in mice. J Immunother Cancer, 2023;11(11).
26. van Niel G, D'Angelo G, Raposo G. Shedding light on the cell biology of extracellular vesicles. Nat Rev Mol Cell Biol. 2018;19(4):213–28.
27. Li RH, et al. A phosphatidic acid-binding LncRNA SNHG9 facilitates LATS1 liquid-liquid phase separation to promote oncogenic YAP signaling. Cell Res. 2021;31(10):1088–105.
28. Liu Y, et al. Identification of a tumour immune barrier in the HCC microenvironment that determines the efficacy of immunotherapy. J Hepatol. 2023;78(4):770–82.
29. Yugawa K, et al. Cancer-associated fibroblasts promote hepatocellular carcinoma progression through downregulation of Exosomal miR-150-3p. Eur J Surg Oncol. 2021;47(2):384–93.
30. Zhang S, et al. Long noncoding RNA NEAT1 changes exosome secretion and MicroRNA expression carried by exosomes in hepatocellular carcinoma cells. J Gastrointest Oncol. 2021;12(6):3033–49.

31. Chen D, et al. LncRNA NEAT1 suppresses cellular senescence in hepatocellular carcinoma via KIF11-dependent repression of CDKN2A. Clin Transl Med. 2023;13(9):e1418.
32. Mehta S, Zhang J. Liquid-liquid phase separation drives cellular function and dysfunction in cancer. Nat Rev Cancer. 2022;22(4):239–52.
33. Tong X, et al. Liquid-liquid phase separation in tumor biology. Signal Transduct Target Ther. 2022;7(1):221.
34. Wang B, et al. Liquid-liquid phase separation in human health and diseases. Signal Transduct Target Ther. 2021;6(1):290.
35. Lu B, et al. Pharmacological Inhibition of core regulatory circuitry Liquid-liquid phase separation suppresses metastasis and chemoresistance in osteosarcoma. Adv Sci (Weinh). 2021;8(20):e2101895.
36. Yamazaki T, Yamamoto T, Hirose T. Micellization: A new principle in the formation of biomolecular condensates. Front Mol Biosci. 2022;9:974772.
37. Bouchard JJ, et al. Cancer mutations of the tumor suppressor SPOP disrupt the formation of active, Phase-Separated compartments. Mol Cell. 2018;72(1):19–e368.
38. Kiang KM, et al. Biomolecular condensates: hubs of Hippo-YAP/TAZ signaling in cancer. Trends Cell Biol. 2024;34(7):566–77.
39. Nozawa RS, et al. Nuclear microenvironment in cancer: control through liquid-liquid phase separation. Cancer Sci. 2020;111(9):3155–63.
40. Peran I, Martin EW, Mittag T. Walking along a protein phase diagram to determine coexistence points by static light scattering. Methods Mol Biol. 2020;2141:715–30.
41. Chiariello AM, Corberi F, Salerno M. The interplay between phase separation and Gene-Enhancer communication: A theoretical study. Biophys J. 2020;119(4):873–83.
42. Wang C, et al. Stress induces dynamic, Cytotoxicity-Antagonizing TDP-43 nuclear bodies via paraspeckle LncRNA NEAT1-Mediated Liquid-Liquid phase separation. Mol Cell. 2020;79(3):443–e4587.
43. Hirose T, Yamazaki T, Nakagawa S. Molecular anatomy of the architectural NEAT1 noncoding RNA: the domains, interactors, and biogenesis pathway required to build phase-separated nuclear paraspeckles. Wiley Interdiscip Rev RNA. 2019;10(6):e1545.
44. Ramasamy T, et al. Nano drug delivery systems for antisense oligonucleotides (ASO) therapeutics. J Control Release. 2022;352:861–78.
45. Mahpour A, Mullen AC. Our emerging Understanding of the roles of long non-coding RNAs in normal liver function, disease, and malignancy. JHEP Rep. 2021;3(1):100177.

Publisher's note